ACS APPLIED MATERIALS & INTERFACES

Research Article

www.acsami.org

Three-Dimensional Heterostructures of MoS_2 Nanosheets on Conducting MoO_2 as an Efficient Electrocatalyst To Enhance Hydrogen Evolution Reaction

Revannath Dnyandeo Nikam,[†,‡,§,@] Ang-Yu Lu,[∥,@] Poonam Ashok Sonawane,[⊥,#] U. Rajesh Kumar,[†,‡,§] Kanchan Yadav,[†,‡,§] Lain-Jong Li,[*,∥] and Yit-Tsong Chen[*,†,‡]

[†]Department of Chemistry, National Taiwan University, Taipei 106, Taiwan

[‡]Institute of Atomic and Molecular Sciences, Academia Sinica, Taipei 106, Taiwan

[§]Nanoscience and Technology Program, Taiwan International Graduate Program, Academia Sinica, Taipei 115, Taiwan

[∥]Division of Physical Science & Engineering, King Abdullah University of Science and Technology , Thuwal 23955-6900, Kingdom of Saudi Arabia

[⊥]Institute of Chemistry, Academia Sinica, Taipei 115, Taiwan

[#]Department of Applied Chemistry, National Chiao-Tung University, Hsinchu 300, Taiwan

Supporting Information

ABSTRACT: Molybdenum disulfide (MoS_2) is a promising catalyst for hydrogen evolution reaction (HER) because of its unique nature to supply active sites in the reaction. However, the low density of active sites and their poor electrical conductivity have limited the performance of MoS_2 in HER. In this work, we synthesized MoS_2 nanosheets on three-dimensional (3D) conductive MoO_2 via a two-step chemical vapor deposition (CVD) reaction. The 3D MoO_2 structure can create structural disorders in MoS_2 nanosheets (referred to as 3D MoS_2/MoO_2), which are responsible for providing the superior HER activity by exposing tremendous active sites of terminal disulfur of S_2^{-2} (in MoS_2) as well as the backbone conductive oxide layer (of MoO_2) to facilitate an interfacial charge transport for the proton reduction. In addition, the MoS_2 nanosheets could protect the inner MoO_2 core from the acidic electrolyte in the HER. The high activity of the as-synthesized 3D MoS_2/MoO_2 hybrid material in HER is attributed to the small onset overpotential of 142 mV, a largest cathodic current density of 85 mA cm^{-2}, a low Tafel slope of 35.6 mV dec^{-1}, and robust electrochemical durability.

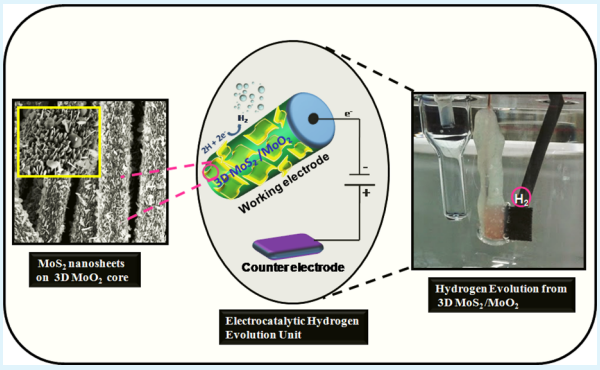

KEYWORDS: *CVD growth, 3D heterostructures, MoS_2 nanosheets, 3D MoO_2 conductive core, electrocatalyst, hydrogen evolution reaction*

1. INTRODUCTION

Due to the massive demand of energy, hydrogen fuel has been proposed as a main future energy resource.[1−3] Beyond the conventional hydrogen production, a lot of effort has been made recently to develop electrocatalytic and photocatalytic techniques to produce efficient hydrogen through the hydrogen evolution reaction (HER).[4−7] However, the existence of high operating overpotential for HER limits the practical applications of these techniques; therefore, developing high-performance catalysts to drive HER with minimum external energy is highly desirable. Platinum (Pt) is well-known for its superior electrocatalytic property; nevertheless, large-scale application of Pt-based technology is hindered by high cost and low availability. Hence, intensive research has recently been directed to search for earth abundant, low-cost potential substitutes for the Pt catalyst. Among the newly discovered catalysts, two-dimensional layered transition metal dichalcogenides (TMDs) have emerged as promising electrocatalysts for HER.[8−12]

In TMDs, molybdenum disulfide (MoS_2) has shown to be an excellent HER catalyst.[8] The computational and experimental results confirmed that the active catalytic sites of layered MoS_2 crystals are located at the sulfur edge, while basal planes are catalytically inert.[13,14] Notwithstanding, due to high surface energy and strong interlayer $\pi-\pi$ interaction, the inherent layer stacking and agglomeration in MoS_2 decrease the number of active sites.[15] In addition, the very poor electrical conductivity between two stacked S−Mo−S interlayers are about 2 orders of magnitude lower than that of intralayers.[16,17] Therefore,

Received: August 26, 2015
Accepted: October 5, 2015
Published: October 5, 2015

DOI: 10.1021/acsami.5b07960
ACS Appl. Mater. Interfaces 2015, 7, 23328−23335

seeking advanced structural designs to engineer the morphological MoS_2 of more active sites for higher conductivity to enhance the electrocatalytic efficiency of MoS_2 in HER is highly demanded.

To overcome the conductivity barrier, MoS_2 has been grown on various conductive carbon-based substrates in recent years, such as graphene nanosheets,[8] ^{18}N-doped graphene,[19] carbon nanotube,[20,21] carbon fiber,[22] carbon cloth,[23] three-dimensional (3D) hierarchical graphene oxide,[24] and graphene protected 3D Ni foam.[25,26] However, the direct deposition of MoS_2 on nonactive HER substrates would block the active sites of MoS_2, thus significantly decreasing the HER activity. Alternatively, enormous effort has been taken to create efficient active sites by making different nanostructures of MoS_2, such as mesopores,[18] chemically exfoliated 1T metallic nanosheets,[27,28] amorphous nanosheets,[29−31] oxygen-doped nanosheets,[32,33] defect-rich nanosheets,[34] nanowires,[35] monolayer 3D nonoporous golds,[36] nanosheets on porous MoO_2,[37] nitrogen-doped nanosheets on MoO_2 nanobelts,[38] and nanoparticles on TCNQ.[39] Among these, the recently developed phase-transfer strategy of producing metallic 1T MoS_2 from semiconductive 2H MoS_2 has significantly improved the HER activity due to the low resistance and high density of active sites in the metallic 1T MoS_2. However, both the complicated synthetic procedures and the instability in the acidic electrolyte of 1T MoS_2 have made it less possible to become an ideal catalyst for HER. Although the previously reported morphological and structural modifications of MoS_2 are still insufficient to enhance the HER activity, an unprecedented 3D MoS_2/MoO_2 hybrid material synthesized by controlling the conductivity and disorder in MoS_2 nanosheets coated on a 3D conductive MoO_2 core could make the practical implementation of MoS_2 for electrocatalytic hydrogen production in HER. The development of 3D architectures of the MoS_2-based catalyst on a conducting substrate is of great interest due to their unique structure-dependent properties. More recently, a template-assisted wet-chemical approach to grow 3D MoS_2 on a conducting substrate has been developed, where the 3D assembled structures acted as an excellent catalyst for HER with high activity and stability.[40,41] Nevertheless, the mass production of such high-quality 3D architectures of MoS_2 demands a new method for large-scale synthesis. Herein, we propose an innovative approach to selectively grow a 3D heterostructure of MoS_2 on a conducting substrate, such as MoO_2. The formation of such 3D heterostructures via a CVD reaction represents a completely new approach. In this paper, we demonstrate that the as-fabricated 3D hybrid heterostructures of MoS_2 nanosheets on a conductive MoO_2 core have several advantages to boost the HER activity. First, MoS_2 nanosheets act as a protective layer for the underlying 3D MoO_2 core from the environmental acidic electrolyte in HER, conferring the 3D MoS_2/MoO_2 hybrid material higher stability. Second, the 3D MoS_2/MoO_2 structure possesses a high specific surface area. Third, the underlying 3D conductive MoO_2 core allows the effective charge collection and charge transfer for a proton reduction reaction. Finally, the 3D MoO_2 architecture can create structural disorders in MoS_2 nanosheets, which are responsible for exposing tremendous active sites of terminal S_2^{2-} to facilitate the HER.

2. EXPERIMENTAL SECTION

2.1. Synthesis of 3D MoS_2/MoO_2 Catalysts. The 3D MoS_2/MoO_2 heterostructures were synthesized in a low-pressure chemical vapor deposition (LPCVD) reaction. The distorted MoS_2 nanosheets on metallic 3D MoO_2 were produced by low-temperature sulfurization in a two-step CVD process as illustrated in Figure 1. The commercially

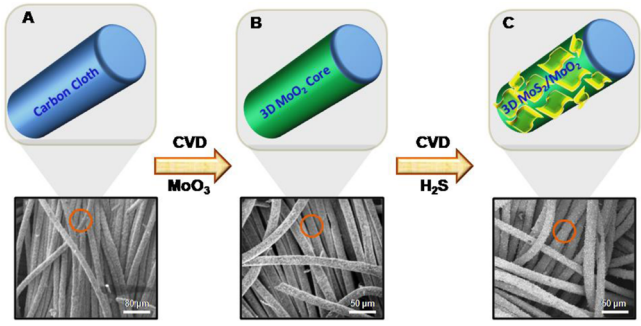

Figure 1. Schematic representations and SEM images illustrate a synthetic process of the designed MoS_2 nanosheets coated on a metallic 3D MoO_2 core, which is supported on carbon cloth, to be used as an electrode for HER. (A) Pristine carbon cloth, (B) metallic 3D MoO_2 on the carbon cloth via the CVD reaction of MoO_3, and (C) MoS_2 nanosheets deposited on the metallic 3D MoO_2 core/carbon cloth (to form 3D MoS_2/MoO_2) by controlling the sulfurization of the pregrown MoO_2 core.

available carbon cloth (CeTech, W0S1002) was used as a template to grow metallic 3D MoO_2 cores. Before the synthesis, MoO_3 powder (Sigma-Aldrich, 99.995% 10 mg) as a chemical precursor was placed in a quartz boat close to the central heating zone of a furnace, where a carbon cloth substrate of 2 × 2 cm^2 was placed on top of the quartz boat containing the MoO_3 powder. Before starting the growth, highly pure Ar gas was purged into the furnace for 30 min to make the reaction chamber oxygen-free. The furnace was then heated to 650 °C at a heating rate of 25 °C/min. During the growth, the chamber pressure was maintained at 5 Torr with an Ar flow rate of 100 sccm. To form distorted MoS_2 nanosheets, the pregrown 3D MoO_2 cores supported by carbon cloth were sulfidized by hydrogen sulfide (H_2S) gas at 100 Torr in another furnace with various reaction temperatures (200−1000 °C) under a ramp rate of 25 °C/min in a mixture of H_2S (4 sccm)/Ar(1000 sccm) for 60 min.

2.2. Structural Characterizations. Powder X-ray diffraction (XRD) patterns of the as-synthesized samples were recorded by a Bruker D8 X-ray diffractometer with Cu Kα (λ = 1.5406 Å) radiation in the 2θ range of 10−80°. Raman spectroscopy was used to identify the compositions of the samples with a confocal Raman microscope (NT-MDT, NTEGRA SPECTRA) and a liquid-nitrogen cooled charge-coupled device (CCD) camera. A laser at 488 nm with the spot size of ∼1 μm, adjusted by a 100× objective lens, was used as an excitation source. To avoid sample damage and to gain better spectral resolution, the laser was adjusted to a medium power of 30 mW with the laser exposure time of 10 s. The Raman scattering signal of a silicon substrate at 520 cm^{-1} was used as a reference for calibration. The surface morphologies of the samples were examined by scanning electron microscopy (FEI, Nova 200) equipped with an energy dispersive X-ray (EDX) spectrometer. The microstructural analysis was carried out using high-resolution transmission electron microscope (HRTEM, Tecnai F30) equipped with X-ray energy dispersive spectroscopy (EDS).

2.3. Electrochemical Measurements. Electrochemical studies were carried out in a 3-electrode cell using an AUTOLAB potentiostat (PGSTAT, 302N), where the as-prepared 3D MoS_2/MoO_2 samples coated on a carbon cloth substrate served as the working electrode (WE), an Ag/AgCl (3.0 mol/kg KCl) was used as the reference electrode (RE), and a graphite rod worked as the counter electrode (CE). All of the electrochemical measurements were performed in 0.5 M H_2SO_4 electrolyte. Linear sweep voltammetry was employed to obtain polarization plots with a fixed scan rate of 5 mV/s. The obtained polarization data were calibrated with respect to the

DOI: 10.1021/acsami.5b07960
ACS Appl. Mater. Interfaces 2015, 7, 23328−23335

reversible hydrogen electrode (RHE) by $E_{RHE} = E_{SCE} + 0.28$ V and were reported with an *iR* compensation by $V_{corr} = V - jR_s$, where V_{corr} is the corrected potential for *iR* drop, *j* is polarization current, and R_s is the series resistance. The electrochemical impedance spectra (EIS) were recorded in the frequency range of 102−105 Hz and at the applied amplitude of AC potential of 10 mV. The obtained experimental EIS data were fitted and deconvoluted to an equivalent circuit (2R-CPE circuit model using NOVA 1.9). The Nyquist and Bode plots were recorded from the fitted EIS results.

3. RESULTS AND DISCUSSION

The distorted MoS_2 nanosheets on metallic 3D MoO_2 were produced by low-temperature sulfurization in a two-step CVD process. Figure 1 illustrates the growth process and SEM images of the prepared 3D MoS_2/MoO_2 hybrid structure, which involved two major steps. (A) Deposition of MoO_2 cores on a carbon cloth substrate under an oxygen-free atmosphere to avoid the oxidation of MoO_2. (B) Formation of distorted MoS_2 nanosheets via the stepwise sulfurization of the predeposited 3D MoO_2 by H_2S under an inert Ar atmosphere. For tests, different samples were prepared at various sulfurization temperatures. The SEM images to display the carbon cloth, MoO_2 cores on carbon cloth, and 3D MoS_2/MoO_2 hybrid structures are shown in Figure 1. Briefly, the formation mechanism of the layered MoS_2/MoO_2 structures is based on a controlled reduction and sulfurization process. In this method, underlying MoO_2 cores were first synthesized on the 3D carbon cloth by the thermal reduction of MoO_3 powder in an inert Ar atmosphere at 650 °C. The surface sulfurization of crystalline MoO_2 cores by H_2S produces the top MoS_2 nanosheets at various temperatures, where the efficiency of sulfurization depends on the diffusion rate of H_2S gas. Therefore, the structures and sizes of the underlying MoO_2 cores and MoS_2 nanosheets can be controlled via the layer-by-layer sulfurization by adjusting the sulfurization conditions.

Figure 2A shows the XRD patterns of the as-prepared samples of MoO_2, 3D MoS_2/MoO_2, and MoS_2. From the XRD patterns, it is clear that the sulfurization temperature has an important effect on the crystallinity of a catalyst. For the unsulfidized 3D MoO_2 sample, Figure 2A(a) shows the pure crystalline MoO_2 (JCPDS:32-0671, monoclinic) with the characteristic diffraction peaks at 40° (120), 43° (112), 58° (031), and 73° (131). As the sulfurization temperature was raised to 300 °C [Figure 2A(b)], in addition to MoO_2, several medium-weak peaks appeared at 14.3°, 33.1°, and 60.4°, corresponding to MoS_2 (003), (101), and (113), respectively (JCPDS: 65-3656, hexagonal). These results suggest that the 3D MoS_2/MoO_2 hybrid structure could be formed at 300 °C. Figure 2A(c) further shows that pure MoS_2 was obtained at 1000 °C, where only the diffraction peaks at 14.3° (003), 33.1° (101), and 60.4° (113) were observed, indicating the disappearance of the MoO_2 core. These results demonstrate that the transition of 3D MoS_2/MoO_2 to crystalline MoS_2 can be adjusted by the sulfurization temperature.

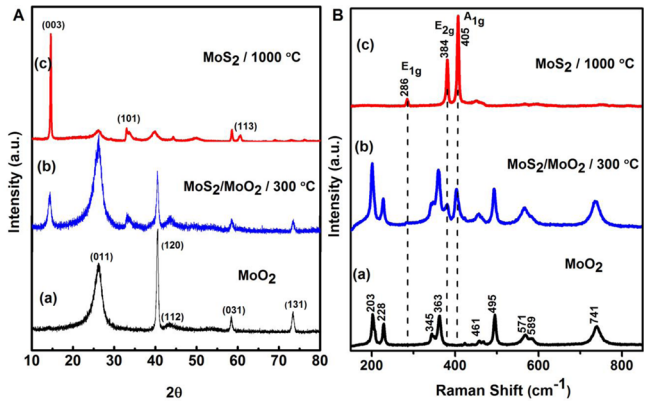

Figure 2. (A) XRD patterns of (a) the unsulfidized 3D MoO_2 core with crystalline planes of MoO_2, (b) 3D MoS_2/MoO_2 structure of both MoS_2 and MoO_2 crystals, and (c) MoS_2 crystalline planes. (B) Raman spectra recorded under 488 nm excitation for (a) the unsulfidized 3D MoO_2 core, (b) 3D MoS_2/MoO_2 core where the appearance of new bands are attributed to MoS_2 as marked by dashed lines, and (c) pure MoS_2 with the identified E_{1g}, E_{2g}, and A_{1g} phonon modes.

The as-prepared samples were also characterized by Raman spectroscopy as shown in Figure 2B. Thermal deposition of MoO_3 on the carbon cloth substrate leads to the formation of metallic MoO_2 cores through the thermal reduction of MoO_3. In Figure 2B(a), Raman signals of the unsulfidized 3D metallic MoO_2 core comprise those of the reported rutile MoO_2 crystal,[42] where the peaks at 203−495 cm^{-1} are assigned to the stretching modes of the doubly coordinated oxygen (Mo−O−Mo) and the signals at 571, 589, and 741 cm^{-1} are due to the stretching modes of terminal oxygen (M═O). This Raman identification of the unsulfidized MoO_2 sample suggests the presence of tetrahedral co-ordination on the Mo^{2+} (i.e., metallic 3D MoO_2) center, which is subjected to sulfurization by H_2S at various temperatures from 200 to 1000 °C. When the sulfurization temperature was increased to 300 °C [Figure 2B(b)], accompanying with the original signals of MoO_2 are new emerging peaks at ∼384 and 405 cm^{-1}, corresponding to the E^1_{2g} (the in-plane vibration of the S atoms) and A_{1g} (the out-of-plane vibration of the S atoms) modes of MoS_2, respectively.[43] This outcome confirms that the partial sulfurization of 3D MoO_2 core occurred at 300 °C, leading to the formation of the 3D MoS_2/MoO_2 hybrid structure. At higher sulfurization temperature of 1000 °C [Figure 2B(c)], all peaks of the MoO_2 core disappeared, transforming to the complete formation of MoS_2 on the carbon cloth substrate. The detailed spectral analyses of the observed Raman bands are listed in Table S1.

The surface morphologies of MoO_2, 3D MoS_2/MoO_2, and MoS_2 on carbon cloth were further investigated by scanning electron microscopy (SEM). Figure 3A shows the high- and low-magnification SEM images of 3D MoO_2 cores, indicating that the entire surface of the carbon cloth was uniformly covered with MoO_2 cores of ∼100 nm in thickness. After the sulfurization temperature was increased to 300 °C, it can be seen from Figure 3B that the MoO_2 surfaces were decorated with MoS_2 nanosheets of ∼22 nm in thickness and ∼50 nm in length. This result provides a strong evidence of forming distorted MoS_2 nanosheets on the 3D MoO_2 core. As revealed from Figure 3C, the distorted MoS_2 nanosheets were converted into continuous MoS_2 layers by raising the sulfurization temperature to 1000 °C and the MoO_2 cores also turned completely into MoS_2 layers. In Figure 3D, the SEM image and EDX elemental mappings of the as-prepared 3D MoS_2/MoO_2 hybrid structure obtained at 300 °C reveal uniform distributions of the Mo, O, and S elements. In comparison, while the EDX mapping of the unsulfidized MoO_2 in Figure S1 contains the elements of Mo and O, the MoS_2 sample was obtained only at 1000 °C as shown in Figure S2. The results from EDX elemental mapping are consistent with those

DOI: 10.1021/acsami.5b07960
ACS Appl. Mater. Interfaces 2015, 7, 23328−23335

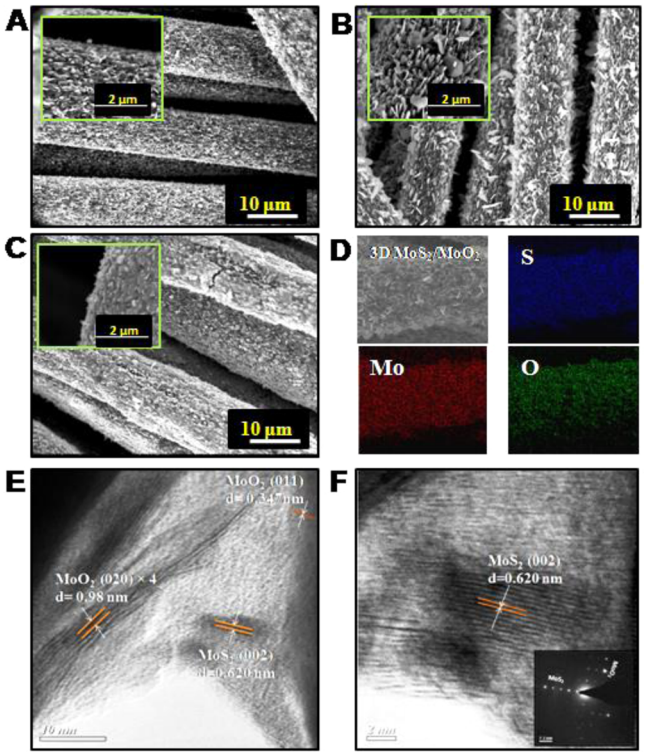

Figure 3. SEM images of (A) MoO_2 on carbon cloth synthesized at 650 °C, (B) 3D MoS_2/MoO_2 on carbon cloth synthesized at 300 °C, and (C) MoS_2 on carbon cloth synthesized at 1000 °C. All insets in (A–C) show the corresponding high-magnification SEM images. (D) EDX elemental mapping images of Mo, S, and O for the 3D MoS_2/MoO_2. (E) HRTEM image of the 3D MoS_2/MoO_2. (F) HRTEM image of a selected MoS_2 region. The inset shows a selected-area electron diffraction (SAED) pattern for the 3D MoS_2/MoO_2.

obtained from XRD and Raman spectroscopy. Microstructural characterization of the 3D MoS_2/MoO_2 heterostructures was performed with HRTEM. Figure 3E displays an HRTEM image of the 3D MoS_2/MoO_2 heterostructure, where MoS_2 layers grew vertically on the 3D MoO_2 backbone. Figure 3F shows an HRTEM image taken in the middle of this 3D MoS_2/MoO_2 heterostructure. Several sheet-like MoS_2 layers of ∼20 nm in length and several nanometers in width were observed to be closely packed on the top of MoO_2 layers. The HRTEM image of a selected MoS_2 region (Figure 3E) reveals the individual atomic planes ordered in the S–Mo–S sequence for the layer formation. The layer spacings can be determined to be ∼0.620 nm for MoS_2 (002), ∼0.980 nm for MoO_2 (020 × 4), and ∼0.347 nm for MoO_2 (011), which are in good agreement with the lattice spacings of MoS_2 and MoO_2 crystals.[37] To provide a further insight into the structural and morphological features of the obtained 3D MoO_2 core, transmission electron microscopic (TEM) characterizations were performed. Figure S3A and S3B show the low-magnification TEM images for the detached MoO_2 core from the carbon cloth by ultrasonication. It is interesting that spiral 3D morphological ultrathin layers of MoO_2 cores were observed after detaching from the 3D template.

To investigate the valence states and surface chemical compositions of MoO_2, 3D MoS_2/MoO_2, and MoS_2, high-resolution X-ray photoemission spectroscopy (XPS) was performed. Figure 4 shows the XPS spectra scanned in the Mo 3d and S 2p regions of MoO_2, 3D MoS_2/MoO_2, and MoS_2.

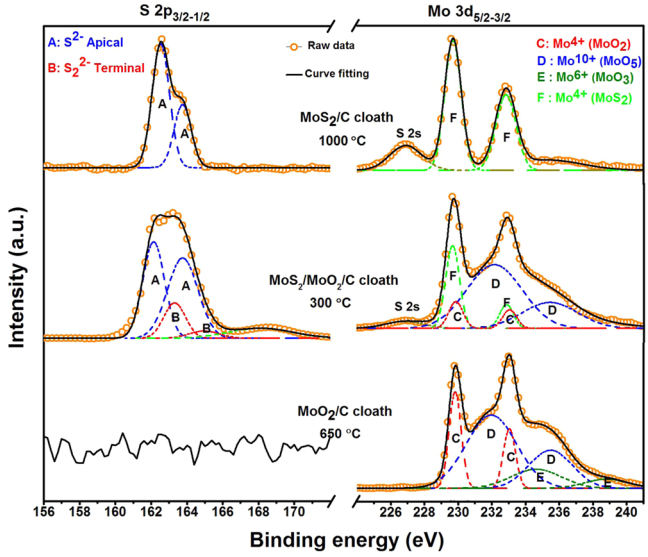

Figure 4. XPS spectra at high-resolution scans of the Mo $3d_{5/2-3/2}$ and S $2p_{3/2-1/2}$ regions for the 3D MoO_2, 3D MoS_2/MoO_2, and MoS_2 catalysts grown on carbon cloth. In the S $2p_{3/2-1/2}$ region, the doublet A, corresponding to the apical S^{2-} at the lower-energy side (162.1–163.3 eV), partially overlap the doublet B, attributed to the bridging S_2^{2-} at the higher-energy side (163.7–164.9 eV). In the Mo $3d_{5/2-3/2}$ region, the doublet C is due to the Mo^{4+} in MoO_2 (229.8–233.04 eV), doublet D is Mo^{10+} in MoO_5 (231.9–234.6 eV), doublet E is Mo^{6+} in MoO_3 (235.4–238.7 eV), and doublet F is Mo^{4+} in MoS_2 (229.6–232.8 eV).

It is well-known that the apical divalent sulfide ions (S^{2-}) in MoS_2 act as active sites in HER;[31,44] moreover, recent studies reported that the presence of terminal S_2^{2-}, in addition to S^{2-}, boosts the HER activity. In XPS spectra, the S $2p_{3/2}$ and $2p_{1/2}$ signals of terminal S_2^{2-} (denoted by doublet B) at 163.7–164.9 eV are located at higher binding energies than those of apical S^{2-} (represented as doublet A) at 162.1–163.3 eV.[14,45] In Figure 4, the MoO_2 core to facilitate the formation of apical S^{2-} ions is confirmed by the presence of doublet A in XPS spectra, where the signals were deconvoluted. The analysis from Figure 4 shows that 3D MoS_2/MoO_2 has both terminal S_2^{2-} (doublet B) and apical S^{2-} (doublet A). It is interesting to observe that the signals of S_2^{2-} (doublet B) almost disappeared in MoS_2 because of the high crystalline phase of MoS_2. Also in Figure 4, the unsulfidized MoO_2 sample does not possess S^{2-} and S_2^{2-}. The ratios of apical S^{2-} to terminal S_2^{2-} for MoO_2, 3D MoS_2/MoO_2, and MoS_2 are summarized in Table S2. These XPS results suggest that the presence of terminal S_2^{2-} could be the main cause to enhance the HER activity in 3D MoS_2/MoO_2.

In the XPS analysis, the Mo 3d orbital splits into $3d_{3/2}$ (higher energy) and $3d_{5/2}$ (lower energy) due to the spin–orbital splitting. In MoO_2, the doublets are at 229.8 eV for Mo^{4+} $3d_{5/2}$ and at 233.04 eV for Mo^{4+} $3d_{3/2}$.[46] After the complete reduction of MoO_3, the characteristic doublets at 235.4–238.7 eV for MoO_3 were not observed; however, due to the slight surface oxidation of the metastable MoO_2 in air, doublets for the Mo^{6+} (235.4–238.7 eV) of MoO_3 were detected.[47,48] In the 3d regions of the Mo ions, the main $3d_{5/2}$ and $3d_{3/2}$ peaks were further analyzed with several doublets of Mo^{4+} (peak C, at 229.8–233.04 eV) for MoO_2, Mo^{10+} (peak D, at 231.9–234.6 eV) for MoO_5, Mo^{4+} (peak E, at 229.6–232.8 eV) for MoS_2, and Mo^{6+} (peak F, at 235.4–238.7 eV) for MoO_3. Each doublet was deconvoluted with a fixed peak

DOI: 10.1021/acsami.5b07960
ACS Appl. Mater. Interfaces 2015, 7, 23328–23335

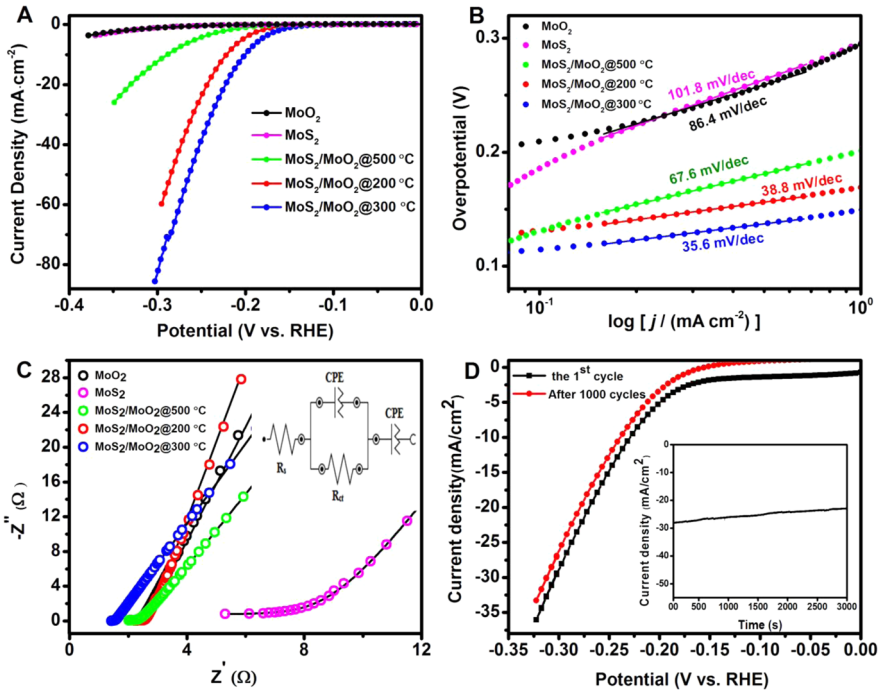

Figure 5. (A) The *iR* corrected polarization curves recorded at the scan rate of 5 mV s^{-1} for the HER containing 0.5 M H_2SO_4 with the unsulfidized 3D MoO_2, 3D MoS_2/MoO_2 (prepared at 200 °C CVD), 3D MoS_2/MoO_2 (prepared at 300 °C CVD), 3D MoS_2/MoO_2 (prepared at 500 °C CVD), and MoS_2, respectively. (B) The corresponding Tafel plots with the data being derived from (A). (C) The Nyquist plots and an equivalent circuit of the unsulfidized MoO_2, 3D MoS_2/MoO_2 (200 °C), 3D MoS_2/MoO_2 (300 °C), 3D MoS_2/MoO_2 (500 °C), and MoS_2 at a potential of −200 mV (vs RHE). (D) Stability test for the 3D MoS_2/MoO_2 (300 °C).

separation of 3.2 eV, intensity ratio ($3d_{5/2}$: $3d_{3/2}$) of 3:2, and the same full width at half-maximum (FWMH).

The XPS results for the unsulfidized MoO_2 sample (Figure 4) clearly show that peak intensities for the reduced states of Mo^{4+} $3d_{3/2}$ and $3d_{5/2}$ from MoO_2 (peak C) and of Mo^{10+} $3d_{3/2}$ and $3d_{5/2}$ from MoO_5 (peak D) are much higher than those of Mo^{6+} $3d_{3/2}$ and $3d_{5/2}$ of MoO_3 (peak E), suggesting a complete reduction of MoO_3 to MoO_2. Similarly, Figure 4 also presents the 3d Mo regions for 3D MoS_2/MoO_2 and MoS_2. In both spectra, the new S 2*s* peak at 226.7 eV (peak F) belongs to MoS_2, indicating the formation of MoS_2. For 3D MoS_2/MoO_2 sample, fractional percentages of the oxidation states of +4 (MoO_2), +10 (MoO_5), +4 (MoS_2), and +6 (MoO_3) were measured to be 8.04%, 61.89%, 18.3%, and 8.31%, respectively, which confirmed the formation of the MoS_2/MoO_2 core. In the formation of MoS_2, while the fractional percentages of +4 (MoO_2), +10 (MoO_5), and +6 (MoO_3) reduced to 0%, 0%, and 16.09%, respectively, the intensity of +4 (MoS_2) increased to 68.73%. In Table S3, the ratios of Mo^{4+} (MoS_2)/Mo^{4+} (MoO_2) and of Mo^{4+} (MoO_2)/Mo^{6+} (MoO_3) were estimated for all samples. Additionally, the results obtained from the XPS analysis are summarized in Figure S4 and are also correlated with the results collected from the EDX spectral analysis in Figure S5. The results obtained from XPS, consistent well with those of EDX, clearly show that the formation of MoS_2 on the 3D MoO_2 core through sulfurization was carried out at 300 °C, of which the as-prepared samples possess high percentage of active sites of apical S^{2-} and terminal S_2^{2-}. Additionally, the structure and composition of the 3D MoS_2/MoO_2 prepared at 500 °C were investigated by SEM, EDX, and XPS. The observed SEM (Figure S6A) shows that parts of the sample peeled off from the original substrate due to the high sulfurization rate and reveals that almost all of the underlying MoO_2 was converted to MoS_2. The XPS analyses (Figure S6, F−G) on both Mo 3d and S 2p regions indicate that this sample contains +10 (MoO_5), +4 (MoS_2), and apical S^{2-}, which are consistent with the EDX examination (Figures S6, B−D).

The electrocatalytic HER activities for the samples prepared above were conducted in a 3-electrode cell containing 0.5 M H_2SO_4. Figure 5A shows the polarization curve of the HER between −0.4 and 0.0 V vs RHE (*iR* corrected) at the scan rate of 5 mV/s for MoO_2, 3D MoS_2/MoO_2, and MoS_2, which were deposited on the carbon cloth with the same loading of ∼0.30 mg/cm^2. While the unsulfidized MoO_2 and the completely sulfidized MoS_2 exhibited poor catalytic activity for HER (with small cathodic currents at η = 300 mV), the as-prepared 3D MoS_2/MoO_2 (at 300 °C) hybrid electrode could provide an extremely large cathodic current density of 85 mA cm^{-2} at η = 300 mV. As shown in Figure S7, compared with MoO_2 and MoS_2, 3D MoS_2/MoO_2 holds a much lower onset potential of 142 mV. This small onset potential and higher cathodic current density yield a superior HER activity, which can be attributed to the distorted structures of MoS_2 nanosheets assembled on the metallic 3D MoO_2 core. It is widely accepted that the HER active sites are located on the edge planes; therefore, the HER activity can be greatly enhance by tailoring the MoS_2 microstructures to obtain highly exposed edge planes.[49,50] In the present case, the distorted MoS_2 nanosheets assembled on the 3D MoO_2 core possess much more exposed edge planes than pure MoS_2, hence significantly improving the HER activity. However, the sulfurization temperature plays an important role in determining the intrinsic structures and sizes of the MoO_2 core. As shown in Figure 5A, as the sulfurization temperature increases, the HER activity of MoS_2 samples increases first (from 200 to 300 °C), reaches a

DOI: 10.1021/acsami.5b07960
ACS Appl. Mater. Interfaces 2015, 7, 23328−23335

maximum value at 300 °C, and then drops sharply afterward (from 300 to 500 °C). The catalysts obtained at low temperatures generally contain rich defects, which can provide more active sites and are beneficial to the HER activity. Nevertheless, defects are also detrimental to the in-layer conductivity of MoS_2. Therefore, a balance between active sites and conductivity is necessary to obtain an optimal condition. As temperature increases, the crystallinity of the catalysts is generally improved, inferring less defects and better conductivity. As a result, the activity is enhanced gradually by increasing temperature from 200 to 300 °C but decreases at higher temperature.

The Tafel slope, the inherent property of an electrocatalyst, can be determined by the rate-limiting step of HER. In Figure 5B, the Tafel slope was calculated from the linear portion of the Tafel plots by fitting the experimental data to the Tafel equation of $\eta = b \log j + a$, where j is the current density and b is the Tafel slope. The Tafel slope was estimated to be 86.4 mV/dec, 35.6 mV/dec, and 101.8 mV/dec for MoO_2, 3D MoS_2/MoO_2 (at 300 °C), and MoS_2, respectively. It should be noted that in an acidic medium, three principal steps have been proposed for the conversion of H^+ to H_2, commonly referred to as the Volmer, Heyrovsky, and Tafel reactions with the corresponding Tafel slopes of 120, 40, and 30 mV/dec, respectively.[51,52] The Tafel slope of 35.6 mV/dec for MoS_2/MoO_2 suggests that the HER mechanism proceeds through the Heyrovsky-Tafel reaction. The exchange current density (j_0) is another important HER parameter, which is the intrinsic property of a catalyst to split a water molecule into hydrogen atoms without any external potential. The exchange current densities for MoO_2, 3D MoS_2/MoO_2, and MoS_2 were determined by extrapolating the Tafel plot as shown in Figure S8. The exchange current density for 3D MoS_2/MoO_2 was determined to be 9.0×10^{-4} mA cm^{-2}, which is remarkably higher than those of MoO_2 (1.69×10^{-7} mA cm^{-2}) and MoS_2 (5.4×10^{-7} mA cm^{-2}). To further confirm the role of underlying MoO_2 cores and the enhancing effect of amorphous MoS_2 on the HER activity of 3D MoS_2/MoO_2, samples were synthesized by increasing the sulfurization time from 30 min to 2 h at the same temperature of 300 °C. The HER activities of the as-prepared samples were compared in terms of current density and Tafel slope as shown in Figures S9, A–B. The HER activity decreases sharply with the increasing sulfurization time, which gives a strong evidence that the enhanced HER activity in 3D MoS_2/MoO_2 stems from the conductive underlying MoO_2. We further applied Raman spectroscopy (Figure S9 C) to confirm that the size of the underlying MoO_2 decreases as the sulfurization time increases and all MoO_2 converted completely to MoS_2 after 2 h sulfurization. These results clearly indicate that MoO_2 plays a crucial role in the HER reaction.

The electrochemical impedance spectroscopy (EIS) is an effective technique to investigate the interface reactions and electrode kinetics of the catalysts in HER. Figure 5C shows the representative Nyquist plots of the MoO_2, 3D MoS_2/MoO_2, and MoS_2 electrodes. More detailed analyses were carried out by fitting the impedance data to an equivalent circuit (as depicted in the inset of Figure 5C), where a constant phase element (CPE) was employed. The Nyquist plots reveal a remarkable decrease of the charge-transfer resistance (R_{CT}) from 2.90 Ω (MoS_2) to 0.14 Ω (3D MoS_2/MoO_2), suggesting that the highly conductive MoO_2 substrates could effectively reduce the resistance of the composite catalysts of 3D MoS_2/MoO_2. Moreover, the series resistance (R_s) decreased from 5.35 Ω of MoS_2 to 1.42 Ω of 3D MoS_2/MoO_2. The electrochemical double-layer capacitances (C_{dl}) were also measured to evaluate the effective surface area of various catalysts. The 3D MoS_2/MoO_2 exhibited a much larger C_{dl} of 37.7 μF than the other counterparts, indicating the high exposure of effective active sites. As a consequence, 3D MoS_2/MoO_2 possesses rich effective active sites and high overall conductivity, leading to the superior HER activity.

Besides the HER activity, the stability is another important criterion to evaluate an HER electrocatalyst. To study the stability in acidic environment, the long-term potential cycling stability of 3D MoS_2/MoO_2 was tested by taking a potential scan from −0.4 to 0.1 V for 1000 cycles with an accelerated scanning rate of 100 mV s^{-1}. As depicted in Figure 5D, there is only a slight activity loss after 1000 cycles, manifesting a good durability, consistent with the previous report of a MoS_2-based electrocatalyst. The slight loss of HER activity (Figure 5D) after 1000 cycles may result from the H^+ consumption in the electrolyte, or the remaining H_2 bubbles on the electrode surface, which partially hinders the HER process. From our experiments, this decrease of HER activity can be eliminated by refreshing electrolyte and thoroughly releasing the H_2 bubbles on the electrode. As shown in the inset of Figure 5D, the current density decreased slightly even after 1000 cycles, clearly indicating the superior stability. To further probe the stability of 3D MoS_2/MoO_2 in acidic environment, a continuous HER process was performed at −0.2 V (vs HER). The time-dependent current response for the 3D MoS_2/MoO_2 was measured as presented in the inset of Figure 5D. From the i–t curve, it can be seen that a negligible loss in current density was measured after the continuous operation for 3000 s. As tabulated in Table S4, the remarkable performance metrics of 3D MoS_2/MoO_2 in HER are compared with other previously reported MoS_2-based electrocatalysts. Additionally, the data before and after the iR correction are also provided for comparison in Figure S10.

4. CONCLUSION

In this study, we have developed distorted MoS_2 nanosheets on a 3D MoO_2 metallic core by a two-step CVD process. Such a novel hybrid structure acts as an active catalyst effectively in HER and exhibits an excellent long-term stability with a small overpotential of ∼0.1 V, large cathodic current density (85 mA cm^{-2} at η = 300 mV), and small Tafel slope of 35.6 mV/dec. The metallic 3D MoO_2 core, formed by the partial reduction of MoO_3, serves as a highly conductive layer, which facilitates the fast charge transport and collection; meanwhile, the distorted MoS_2 nanosheets play the role of an HER catalyst with tremendous amount of exposed active sites and also protect the inner MoO_2 core from an acidic electrolyte. The excellent electrocatalytic performance of 3D MoS_2/MoO_2 potentially enables this hybrid structure to replace the high-cost Pt catalyst.

■ ASSOCIATED CONTENT

Supporting Information

The Supporting Information is available free of charge on the ACS Publications website at DOI: 10.1021/acsami.5b07960.

Figures S1–S10 (EDX, TEM, SEM, XPS, and detailed electrochemical analysis) and Tables S1–S4 (observed Raman scattering bands, analyses from XPS spectra, and comparison of HER performances (PDF)

DOI: 10.1021/acsami.5b07960
ACS Appl. Mater. Interfaces 2015, 7, 23328–23335

AUTHOR INFORMATION

Corresponding Authors

*E-mail: lance.li@kaust.edu.sa.

*E-mail: ytcchem@ntu.edu.tw.

Author Contributions

[@]R.D.N. and A.-Y.L. contributed equally.

Notes

The authors declare no competing financial interest.

ACKNOWLEDGMENTS

This work was partially supported by the Ministry of Science and Technology (MOST) of Taiwan under MOST 103-2627-M-002-009 and 103-2113-M-002-014-MY3.

REFERENCES

(1) Dresselhaus, M. S.; Thomas, I. L. Alternative Energy Technologies. *Nature* **2001**, *414*, 332−337.

(2) Chu, S.; Majumdar, A. Opportunities and Challenges for a Sustainable Energy Future. *Nature* **2012**, *488*, 294−303.

(3) Turner, J. A. Sustainable Hydrogen Production. *Science* **2004**, *305*, 972−974.

(4) Paracchino, A.; Laporte, V.; Sivula, K.; Grätzel, M.; Thimsen, E. Highly Active Oxide Photocathode for Photoelectrochemical Water Reduction. *Nat. Mater.* **2011**, *10*, 456−461.

(5) Hou, Y.; Abrams, B. L.; Vesborg, P. C. K.; Björketun, M. E.; Herbst, K.; Bech, L.; Setti, A. M.; Damsgaard, C. D.; Pedersen, T.; Hansen, O.; Rossmeisl, J.; Dahl, S.; Nørskov, J. K.; Chorkendorff, I. Bioinspired Molecular co-Catalysts Bonded to a Silicon Photocathode for Solar Hydrogen Evolution. *Nat. Mater.* **2011**, *10*, 434−438.

(6) Desmond Ng, J. W.; Gorlin, Y.; Hatsukade, T.; Jaramillo, T. F. A Precious-Metal-Free Regenerative Fuel Cell for Storing Renewable Electricity. *Adv. Energy Mater.* **2013**, *3*, 1545−1550.

(7) Benck, J. D.; Lee, S. C.; Fong, K. D.; Kibsgaard, J.; Sinclair, R.; Jaramillo, T. F. Designing Active and Stable Silicon Photocathodes for Solar Hydrogen Production Using Molybdenum Sulfide Nanomaterials. *Adv. Energy Mater.* **2014**, *4*, 1400739.

(8) Li, Y.; Wang, H.; Xie, L.; Liang, Y.; Hong, G.; Dai, H. MoS_2 Nanoparticles Grown on Graphene: An Advanced Catalyst for the Hydrogen Evolution Reaction. *J. Am. Chem. Soc.* **2011**, *133*, 7296−7299.

(9) Lin, J.; Peng, Z.; Wang, G.; Zakhidov, D.; Larios, E.; Yacaman, M. J.; Tour, J. M. Enhanced Electrocatalysis for Hydrogen Evolution Reactions from WS_2 Nanoribbons. *Adv. Energy Mater.* **2014**, *4*, 1301875.

(10) Wang, D.-Y.; Gong, M.; Chou, H.-L.; Pan, C.-J.; Chen, H.-A.; Wu, Y.; Lin, M.-C.; Guan, M.; Yang, J.; Chen, C.-W.; Wang, Y.-L.; Hwang, B.-J.; Chen, C.-C.; Dai, H. Highly Active and Stable Hybrid Catalyst of Cobalt-Doped FeS_2 Nanosheets−Carbon Nanotubes for Hydrogen Evolution Reaction. *J. Am. Chem. Soc.* **2015**, *137*, 1587−1592.

(11) Wang, H.; Kong, D.; Johanes, P.; Cha, J. J.; Zheng, G.; Yan, K.; Liu, N.; Cui, Y. $MoSe_2$ and WSe_2 Nanofilms with Vertically Aligned Molecular Layers on Curved and Rough Surfaces. *Nano Lett.* **2013**, *13*, 3426−3433.

(12) Zhang, H.; Yang, B.; Wu, X.; Li, Z.; Lei, L.; Zhang, X. Polymorphic $CoSe_2$ with Mixed Orthorhombic and Cubic Phases for Highly Efficient Hydrogen Evolution Reaction. *ACS Appl. Mater. Interfaces* **2015**, *7*, 1772−1779.

(13) Jaramillo, T. F.; Jørgensen, K. P.; Bonde, J.; Nielsen, J. H.; Horch, S.; Chorkendorff, I. Identification of Active Edge Sites for Electrochemical H_2 Evolution from MoS_2 Nanocatalysts. *Science* **2007**, *317*, 100−102.

(14) Lassalle-Kaiser, B.; Merki, D.; Vrubel, H.; Gul, S.; Yachandra, V. K.; Hu, X.; Yano, J. Evidence from in Situ X-ray Absorption Spectroscopy for the Involvement of Terminal Disulfide in the Reduction of Protons by an Amorphous Molybdenum Sulfide Electrocatalyst. *J. Am. Chem. Soc.* **2015**, *137*, 314−321.

(15) Laursen, A. B.; Kegnaes, S.; Dahl, S.; Chorkendorff, I. Molybdenum Sulfides-Efficient and Viable Materials for Electro - and Photoelectrocatalytic Hydrogen Evolution. *Energy Environ. Sci.* **2012**, *5*, 5577−5591.

(16) Hu, S. Y.; Liang, C. H.; Tiong, K. K.; Lee, Y. C.; Huang, Y. S. Preparation and Characterization of Large Niobium-Doped $MoSe_2$ Single Crystals. *J. Cryst. Growth* **2005**, *285*, 408−414.

(17) Kong, D.; Wang, H.; Cha, J. J.; Pasta, M.; Koski, K. J.; Yao, J.; Cui, Y. Synthesis of MoS_2 and $MoSe_2$ Films with Vertically Aligned Layers. *Nano Lett.* **2013**, *13*, 1341−1347.

(18) Liao, L.; Zhu, J.; Bian, X.; Zhu, L.; Scanlon, M. D.; Girault, H. H.; Liu, B. MoS_2 Formed on Mesoporous Graphene as a Highly Active Catalyst for Hydrogen Evolution. *Adv. Funct. Mater.* **2013**, *23*, 5326−5333.

(19) Hou, Y.; Zhang, B.; Wen, Z.; Cui, S.; Guo, X.; He, Z.; Chen, J. A 3D Hybrid of Layered MoS_2/Nitrogen-Doped Graphene Nanosheet Aerogels: An Effective Catalyst for Hydrogen Evolution in Microbial Electrolysis Cells. *J. Mater. Chem. A* **2014**, *2*, 13795−13800.

(20) Yuan, H.; Li, J.; Yuan, C.; He, Z. Facile Synthesis of MoS_2@CNT as an Effective Catalyst for Hydrogen Production in Microbial Electrolysis Cells. *ChemElectroChem* **2014**, *1*, 1828−1833.

(21) Yan, Y.; Ge, X.; Liu, Z.; Wang, J.-Y.; Lee, J.-M.; Wang, X. Facile Synthesis of Low Crystalline MoS_2 Nanosheet-Coated CNTs for Enhanced Hydrogen Evolution Reaction. *Nanoscale* **2013**, *5*, 7768−7771.

(22) Guo, X.; Cao, G.-l.; Ding, F.; Li, X.; Zhen, S.; Xue, Y.-f.; Yan, Y.-m.; Liu, T.; Sun, K.-n. A Bulky and Flexible Electrocatalyst for Efficient Hydrogen Evolution Based on the Growth of MoS_2 Nanoparticles on Carbon Nanofiber Foam. *J. Mater. Chem. A* **2015**, *3*, 5041−5046.

(23) Yan, Y.; Xia, B.; Li, N.; Xu, Z.; Fisher, A.; Wang, X. Vertically Oriented MoS_2 and WS_2 Nanosheets Directly Grown on Carbon Cloth as Efficient and Stable 3-Dimensional Hydrogen-Evolving Cathodes. *J. Mater. Chem. A* **2015**, *3*, 131−135.

(24) Zhou, W.; Zhou, K.; Hou, D.; Liu, X.; Li, G.; Sang, Y.; Liu, H.; Li, L.; Chen, S. Three-Dimensional Hierarchical Frameworks Based on MoS_2 Nanosheets Self-Assembled on Graphene Oxide for Efficient Electrocatalytic Hydrogen Evolution. *ACS Appl. Mater. Interfaces* **2014**, *6*, 21534−21540.

(25) Chang, Y.-H.; Lin, C.-T.; Chen, T.-Y.; Hsu, C.-L.; Lee, Y.-H.; Zhang, W.; Wei, K.-H.; Li, L.-J. Highly Efficient Electrocatalytic Hydrogen Production by MoSx Grown on Graphene-Protected 3D Ni Foams. *Adv. Mater.* **2013**, *25*, 756−760.

(26) Geng, X.; Wu, W.; Li, N.; Sun, W.; Armstrong, J.; Al-hilo, A.; Brozak, M.; Cui, J.; Chen, T.-p. Three-Dimensional Structures of MoS_2 Nanosheets with Ultrahigh Hydrogen Evolution Reaction in Water Reduction. *Adv. Funct. Mater.* **2014**, *24*, 6123−6129.

(27) Lukowski, M. A.; Daniel, A. S.; Meng, F.; Forticaux, A.; Li, L.; Jin, S. Enhanced Hydrogen Evolution Catalysis from Chemically Exfoliated Metallic MoS_2 Nanosheets. *J. Am. Chem. Soc.* **2013**, *135*, 10274−10277.

(28) Voiry, D.; Salehi, M.; Silva, R.; Fujita, T.; Chen, M.; Asefa, T.; Shenoy, V. B.; Eda, G.; Chhowalla, M. Conducting MoS_2 Nanosheets as Catalysts for Hydrogen Evolution Reaction. *Nano Lett.* **2013**, *13*, 6222−6227.

(29) Shin, S.; Jin, Z.; Kwon, D. H.; Bose, R.; Min, Y.-S. High Turnover Frequency of Hydrogen Evolution Reaction on Amorphous MoS_2 Thin Film Directly Grown by Atomic Layer Deposition. *Langmuir* **2015**, *31*, 1196−1202.

(30) Zhao, X.; Zhu, H.; Yang, X. Amorphous Carbon Supported MoS_2 Nanosheets as Effective Catalysts for Electrocatalytic Hydrogen Evolution. *Nanoscale* **2014**, *6*, 10680−10685.

(31) Merki, D.; Fierro, S.; Vrubel, H.; Hu, X. Amorphous Molybdenum Sulfide Films as Catalysts for Electrochemical Hydrogen Production in Water. *Chem. Sci.* **2011**, *2*, 1262−1267.

(32) Tao, L.; Duan, X.; Wang, C.; Duan, X.; Wang, S. Plasma-Engineered MoS_2 Thin-Film as an Efficient Electrocatalyst for Hydrogen Evolution Reaction. *Chem. Commun.* **2015**, *51*, 7470−7473.

(33) Xie, J.; Zhang, J.; Li, S.; Grote, F.; Zhang, X.; Zhang, H.; Wang, R.; Lei, Y.; Pan, B.; Xie, Y. Controllable Disorder Engineering in

DOI: 10.1021/acsami.5b07960
ACS Appl. Mater. Interfaces 2015, 7, 23328−23335

Oxygen-Incorporated MoS_2 Ultrathin Nanosheets for Efficient Hydrogen Evolution. *J. Am. Chem. Soc.* **2013**, *135*, 17881−17888.
(34) Xie, J.; Zhang, H.; Li, S.; Wang, R.; Sun, X.; Zhou, M.; Zhou, J.; Lou, X. W.; Xie, Y. Defect-Rich MoS_2 Ultrathin Nanosheets with Additional Active Edge Sites for Enhanced Electrocatalytic Hydrogen Evolution. *Adv. Mater.* **2013**, *25*, 5807−5813.
(35) Chen, Z.; Cummins, D.; Reinecke, B. N.; Clark, E.; Sunkara, M. K.; Jaramillo, T. F. Core−shell MoO_3−MoS_2 Nanowires for Hydrogen Evolution: A Functional Design for Electrocatalytic Materials. *Nano Lett.* **2011**, *11*, 4168−4175.
(36) Tan, Y.; Liu, P.; Chen, L.; Cong, W.; Ito, Y.; Han, J.; Guo, X.; Tang, Z.; Fujita, T.; Hirata, A.; Chen, M. W. Monolayer MoS_2 Films Supported by 3D Nanoporous Metals for High-Efficiency Electrocatalytic Hydrogen Production. *Adv. Mater.* **2014**, *26*, 8023−8028.
(37) Yang, L.; Zhou, W.; Hou, D.; Zhou, K.; Li, G.; Tang, Z.; Li, L.; Chen, S. Porous Metallic MoO_2- Supported MoS_2 Nanosheets for Enhanced Electrocatalytic Activity in the Hydrogen Evolution Reaction. *Nanoscale* **2015**, *7*, 5203−5208.
(38) Zhou, W.; Hou, D.; Sang, Y.; Yao, S.; Zhou, J.; Li, G.; Li, L.; Liu, H.; Chen, S. MoO_2 Nanobelts@Nitrogen Self-doped MoS_2 Nanosheets as Effective Electrocatalysts for Hydrogen Evolution Reaction. *J. Mater. Chem. A* **2014**, *2*, 11358−11364.
(39) Chang, Y.-H.; Nikam, R. D.; Lin, C.-T.; Huang, J.-K.; Tseng, C.-C.; Hsu, C.-L.; Cheng, C.-C.; Su, C.-Y.; Li, L.-J.; Chua, D. H. C. Enhanced Electrocatalytic Activity of MoSx on TCNQ-Treated Electrode for Hydrogen Evolution Reaction. *ACS Appl. Mater. Interfaces* **2014**, *6*, 17679−17685.
(40) Zhang, L.; Wu, H. B.; Yan, Y.; Wang, X.; Lou, X. W. Hierarchical MoS_2 Microboxes Constructed by Nanosheets with Enhanced Electrochemical Properties for Lithium Storage and Water Splitting. *Energy Environ. Sci.* **2014**, *7*, 3302−3306.
(41) Yu, X.-Y.; Hu, H.; Wang, Y.; Chen, H.; Lou, X. W. Ultrathin MoS_2 Nanosheets Supported on N-doped Carbon Nanoboxes with Enhanced Lithium Storage and Electrocatalytic Properties. *Angew. Chem., Int. Ed.* **2015**, *54*, 7395−7398.
(42) Dieterle, M.; Weinberg, G.; Mestl, G. Raman Spectroscopy of Molybdenum Oxides Part I. Structural Characterization of Oxygen Defects in MoO_{3-x} by DR UV/VIS, Raman Spectroscopy and X-Ray Diffraction. *Phys. Chem. Chem. Phys.* **2002**, *4*, 812−821.
(43) Lee, Y.-H.; Zhang, X.-Q.; Zhang, W.; Chang, M.-T.; Lin, C.-T.; Chang, K.-D.; Yu, Y.-C.; Wang, J. T.-W.; Chang, C.-S.; Li, L.-J.; Lin, T.-W. Synthesis of Large-Area MoS_2 Atomic Layers with Chemical Vapor Deposition. *Adv. Mater.* **2012**, *24*, 2320−2325.
(44) Vrubel, H.; Hu, X. Growth and Activation of an Amorphous Molybdenum Sulfide Hydrogen Evolving Catalyst. *ACS Catal.* **2013**, *3*, 2002−2011.
(45) Kibsgaard, J.; Jaramillo, T. F.; Besenbacher, F. Building an Appropriate Active-Site Motif into a Hydrogen-Evolution Catalyst with Thiomolybdate $[Mo_3S_{13}]^{2-}$ Clusters. *Nat. Chem.* **2014**, *6*, 248−253.
(46) Schroeder, T.; Zegenhagen, J.; Magg, N.; Immaraporn, B.; Freund, H. J. Formation of a Faceted MoO_2 Epilayer on Mo(112) Studied by XPS, UPS and STM. *Surf. Sci.* **2004**, *552*, 85−97.
(47) Sun, Y.; Hu, X.; Yu, J. C.; Li, Q.; Luo, W.; Yuan, L.; Zhang, W.; Huang, Y. Morphosynthesis of a Hierarchical MoO_2 Nanoarchitecture as a Binder-Free Anode for lithium-Ion Batteries. *Energy Environ. Sci.* **2011**, *4*, 2870−2877.
(48) Yoon, S.; Jung, K.-N.; Jin, C. S.; Shin, K.-H. Synthesis of Nitrided MoO_2 and its Application as Anode Materials for Lithium-Ion Batteries. *J. Alloys Compd.* **2012**, *536*, 179−183.
(49) Smith, A. J.; Chang, Y.-H.; Raidongia, K.; Chen, T.-Y.; Li, L.-J.; Huang, J. Molybdenum Sulfide Supported on Crumpled Graphene Balls for Electrocatalytic Hydrogen Production. *Adv. Energy Mater.* **2014**, *4*, 1400398.
(50) Kibsgaard, J.; Chen, Z.; Reinecke, B. N.; Jaramillo, T. F. Engineering the Surface Structure of MoS_2 to Preferentially Expose Active Edge Sites for Electrocatalysis. *Nat. Mater.* **2012**, *11*, 963−969.
(51) Durst, J.; Siebel, A.; Simon, C.; Hasche, F.; Herranz, J.; Gasteiger, H. A. New Insights into the Electrochemical Hydrogen Oxidation and Evolution Reaction Mechanism. *Energy Environ. Sci.* **2014**, *7*, 2255−2260.
(52) Zheng, Y.; Jiao, Y.; Zhu, Y.; Li, L. H.; Han, Y.; Chen, Y.; Du, A.; Jaroniec, M.; Qiao, S. Z. Hydrogen Evolution by a Metal-Free Electrocatalyst. *Nat. Commun.* **2014**, *5*, 3783.

DOI: 10.1021/acsami.5b07960
ACS Appl. Mater. Interfaces 2015, 7, 23328−23335